

# Large-scale self-assembled nanophotonic scintillators for X-ray imaging

Received: 11 November 2024

Accepted: 5 June 2025

Published online: 01 July 2025

 Check for updates

Louis Martin-Monier <sup>1,9</sup> , Simo Pajovic <sup>2,9</sup> , Muluneh G. Abebe <sup>3,4,9</sup> , Joshua Chen <sup>5</sup>, Sachin Vaidya <sup>3</sup>, Seokhwan Min<sup>3,6</sup>, Seou Choi <sup>5</sup>, Steven E. Kooi <sup>7</sup>, Bjorn Maes <sup>4</sup>, Juejun Hu <sup>1</sup>, Marin Soljačić <sup>3,5</sup> & Charles Roques-Carmes <sup>5,8</sup> 

Scintillators convert X-ray energy into visible light and are critical for imaging technologies. Their widespread use relies on scalable, high-quality manufacturing methods. Nanophotonic scintillators, featuring wavelength-scale nanostructures, can offer improved emission properties such as higher light yield, shorter decay times, and enhanced directionality. However, achieving scalable fabrication of these structures remains challenging. Here, we present a scalable fabrication method for large-area nanophotonic scintillators based on the self-assembly of chalcogenide glass photonic crystals. This technique enables the production of nanophotonic scintillators over wafer-scale areas, achieving a six-fold enhancement in light yield compared to unpatterned scintillators. By studying surface nanofabrication disorder, we show its impact on imaging performance and provide a route towards scintillation enhancements without compromising resolution. We demonstrate the practical applicability of our nanophotonic scintillators through X-ray imaging of biological and inorganic specimens. Our results could enable the industrial implementation of a new generation of nanophotonic-enhanced scintillators.

Scintillation, the process by which certain materials emit light upon exposure to high-energy particles such as X-rays, is paramount to numerous technologies<sup>1</sup>. Its role is particularly prominent in X-ray imaging and characterization, where scintillators are crucial for converting X-ray energy into visible light, which can then be detected and analyzed<sup>2</sup>. Advances in bulk scintillator processing have been key to their widespread adoption in X-ray imaging applications. Techniques like the Czochralski and Bridgman methods<sup>3,4</sup> are highly scalable and have been adapted to produce large, high-quality scintillator crystals in bulk. Other established techniques such as thermal evaporation<sup>5,6</sup> and sol-gel

methods<sup>7</sup> have also been successfully tailored for large-area polycrystalline scintillator manufacturing.

An emerging approach in scintillator research—coined “nanophotonic scintillators”—consists of structuring scintillator materials at the scale of their emission wavelength<sup>8,9</sup> to control their emission properties, such as their light yield<sup>8,10</sup>, emission directionality<sup>11</sup>, detection efficiency<sup>12</sup>, imaging performance<sup>13</sup>, and timing<sup>14</sup>. Such enhancements open up new possibilities for more precise and efficient X-ray imaging technologies<sup>15–17</sup>.

Despite these promising results, the widespread adoption of nanophotonic scintillators is hindered by challenges in scalable

<sup>1</sup>Department of Materials Science and Engineering, MIT, Cambridge, MA, USA. <sup>2</sup>Department of Mechanical Engineering, MIT, Cambridge, MA, USA.

<sup>3</sup>Department of Physics, Massachusetts Institute of Technology, Cambridge, MA 02139, USA. <sup>4</sup>Micro- and Nanophotonic Materials Group, Research Institute for Materials Science and Engineering, University of Mons, 20 Place du Parc, Mons B-7000, Belgium. <sup>5</sup>Research Laboratory of Electronics, MIT, Cambridge, MA, USA. <sup>6</sup>Department of Materials Science and Engineering, Korea Advanced Institute of Science and Technology, Daejeon 34141, Republic of Korea.

<sup>7</sup>Institute for Soldier Nanotechnologies, MIT, Cambridge, MA, USA. <sup>8</sup>E. L. Ginzton Laboratory, Stanford University, 348 Via Pueblo, Stanford, CA 94305, US.

<sup>9</sup>These authors contributed equally: Louis Martin-Monier, Simo Pajovic, Muluneh G. Abebe. ✉ e-mail: [lmartin@mit.edu](mailto:lmartin@mit.edu); [pajovics@mit.edu](mailto:pajovics@mit.edu);

[MulunehGeremew.ABEBE@umons.ac.be](mailto:MulunehGeremew.ABEBE@umons.ac.be); [chrc@stanford.edu](mailto:chrc@stanford.edu)

fabrication techniques. Current top-down fabrication methods, which rely on sophisticated lithographic techniques, offer nanometer-scale resolution and repeatability but are often complex, costly, difficult to scale to large areas<sup>18</sup>, and not transferable to “unconventional” substrate materials such as scintillator crystals. On the other hand, bottom-up approaches such as laser printing<sup>19,20</sup>, chemical or self-assembly methods<sup>21,22</sup>, and topographical control of particle positioning<sup>23</sup> have been explored as alternatives. However, these methods come with their own set of limitations, including throughput constraints, surface defects, roughness, and restricted material choices, which also hinder their practical application. To maximize the technological impact of nanophotonic scintillators, it is imperative to develop fabrication techniques that are scalable to industry-standard detector dimensions (~cm), while preserving enhancements obtained from nanophotonic patterning.

Here, we demonstrate a large-scale nanophotonic scintillator fabrication method that realizes a six-fold nanophotonic enhancement in light yield over centimeter scales. Our method is based on the self-assembly of chalcogenide glass photonic crystals. With the devised method, we realize nanophotonic scintillators over an area of 4 cm × 4 cm (e.g., comparable in length scale to commercial flat panel detectors) with six-fold light yield enhancements compared to a reference bare scintillator. We demonstrate this enhancement in a conventional, and widely used X-ray scintillator material (cerium-doped yttrium aluminum garnet, YAG:Ce). We then elucidate the influence of surface disorder in our nanophotonic scintillator’s imaging performance and obtain large-area scans of biological and inorganic specimens. Our results are poised for rapid integration into industrial applications, enabling a family of optimized nanophotonic-enhanced scintillators for use in medicine, defense, and beyond.

## Results

### Nanophotonic scintillation enhancement over centimeter scales

The depicted fabrication method seamlessly integrates a thin chalcogenide photonic crystal coating atop a scintillating substrate (Fig. 1a, b). Chalcogenide glasses represent a particularly relevant class of materials for nanophotonic scintillation enhancement due their high refractive index ( $2 \leq n \leq 4$ ) and low optical losses from the infrared to

the visible spectrum<sup>24</sup>. Furthermore, thin (sub-100 nm) chalcogenide glass films exhibit viscous behavior during annealing over an extended processing window, making them ideal candidates for templated dewetting processes<sup>25</sup>.

This process begins with the fabrication of a silicon master mold by traditional lithographic techniques (see Methods). Both interference lithography and electron beam lithography are used to make distinct molds, enabling different trade-offs between patterned area and resolution. The sample prepared with electron beam lithography extends over an area 4 mm × 4 mm (“EL” in the rest of this work), while the sample prepared with interference lithography extends over a much larger area of 4 cm × 4 cm (“IL” in the rest of this work). In the next process step, nanoimprint lithography is leveraged to reproduce the master texture onto the bulk scintillator. A polydimethylsiloxane stamp, replicated from a silicon master mold, is pressed onto a UV-curable polymer layer directly on the scintillator substrate and exposed to ultraviolet light (Fig. 1a-1). In a final process step, physical vapor deposition and dewetting is used to obtain a high-index nanoparticle array. A thin layer of chalcogenide glass is deposited using thermal evaporation (Fig. 1a-2). A final glass annealing step above its glass transition temperature induces the re-arrangement of the film into an array of highly ordered nanospheroids (Fig. 1a-3). The precise manipulation of interfacial tension as well as film-texture interaction is instrumental in achieving defect-free nanostructures, as exemplified in Fig. 1d, e. The photonic crystal exhibits a subwavelength period of 450 nm, covering a total patterned area of 4 cm × 4 cm, therefore counting around 10 billion nanoscale spheroids on the chip. Finally, a 15 nm SiO<sub>2</sub> layer is sputtered over the resulting chalcogenide nanoparticle array to avoid further oxidation.

Using a recent framework to model scintillation emission in nanophotonic structures, we anticipate an enhancement in nanophotonic scintillation by amplifying light yield due to better in/out-coupling of light (which maps to an enhancement in non-equilibrium optical absorption in the scintillator layer, via Lorentz reciprocity)<sup>8</sup>, as experimentally observed in Fig. 2a, c. Taking the bare scintillator as reference (no coating nor pattern), our simulations indicate an increase in scintillation light yield of 3.48-fold (EL) and 6.96-fold (IL). These enhancement values are confirmed experimentally, with X-ray

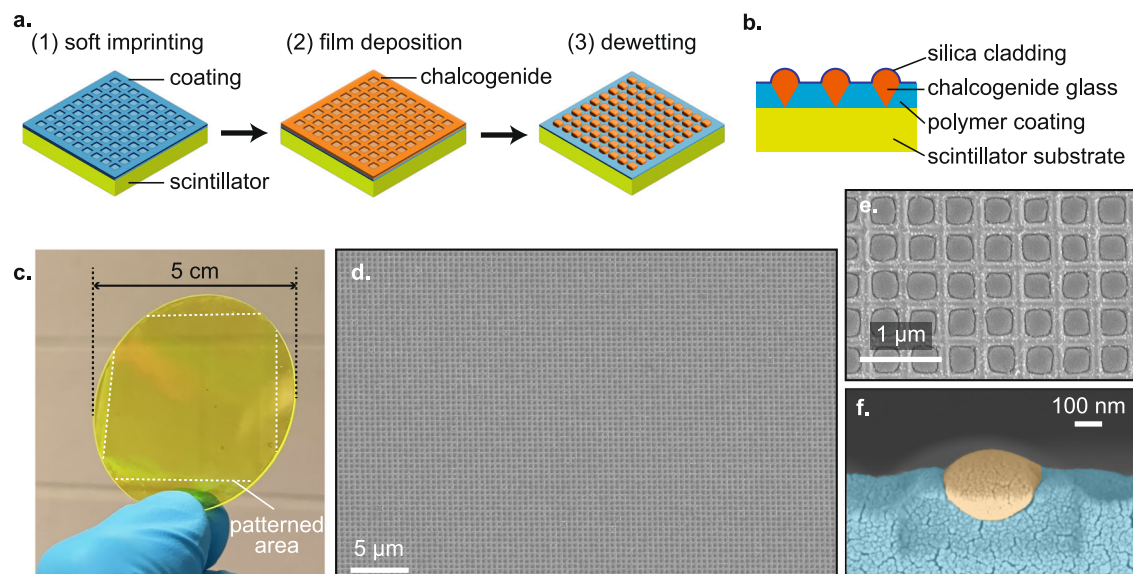
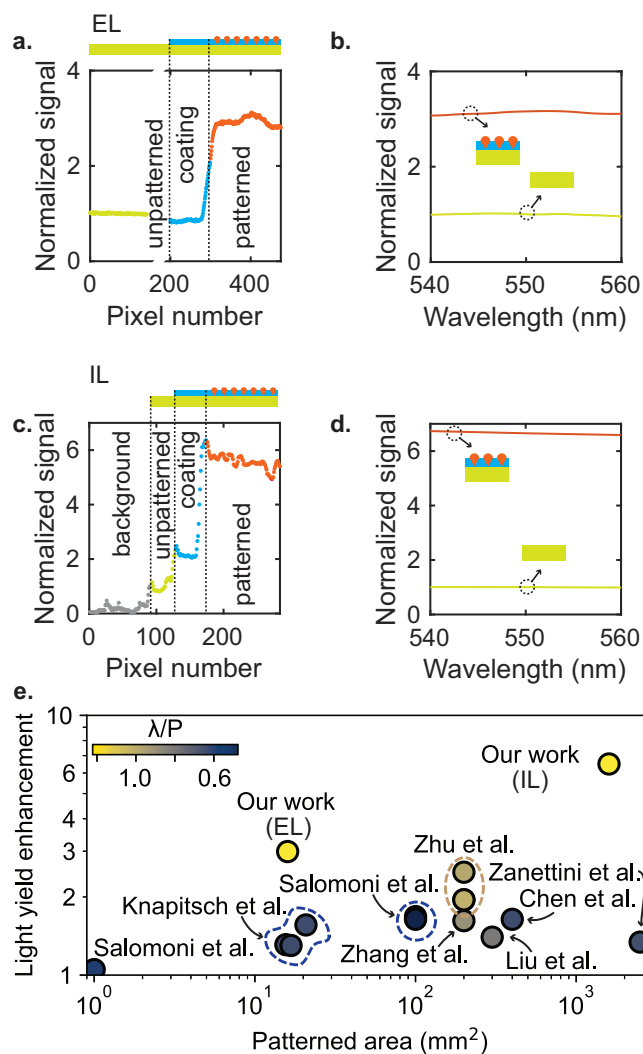


**Fig. 1 | Fabrication scheme of self-assembled nanophotonic scintillators.**

**a** Fabrication method: (1) soft nanoimprinting of polymer coating (blue) spin-coated over scintillator (yellow); (2) chalcogenide film deposition (orange); (3) annealing and dewetting. **b** Cross-sectional schematic of nanophotonic scintillator. **c** Photograph of large scale sample after fabrication of nanostructured layer on a

0.5 mm-thick YAG:Ce scintillator substrate (IL sample). **d** Top view scanning electron micrograph of the dewetted nano-array (IL sample). **e** Zoomed-in top view (IL sample). **f** False color cross-sectional view of a single nanoparticle. From bottom to top, the cross-section shows the polymer coating (blue), a single chalcogenide nanoparticle (orange), and air.



line scans showed in Fig. 2c, d:  $3.00 \pm 0.21$  (EL) and  $6.62 \pm 1.60$  (IL). Since the fabricated structures are spheroids, our numerical simulations consist of a multi-step process that combines finite element methods and rigorous coupled wave analysis<sup>26</sup> (see Methods).

The emission enhancement is associated with the coupling of guided modes to free space plane waves, which creates guided resonances. Consequently, the emission enhancement is proportional to the number of guided resonances, and the subwavelength periodic pattern is critical in achieving optimal enhancement<sup>27,28</sup>. Furthermore, different emission angles may experience different enhancements due to their varying coupling efficiencies. For example, in the region of very large off-normal emission angles, the coupling is weaker and depends on the azimuthal coordinate (decreased enhancement), while at normal and near normal directions, a stronger coupling results in maximum enhancement (see

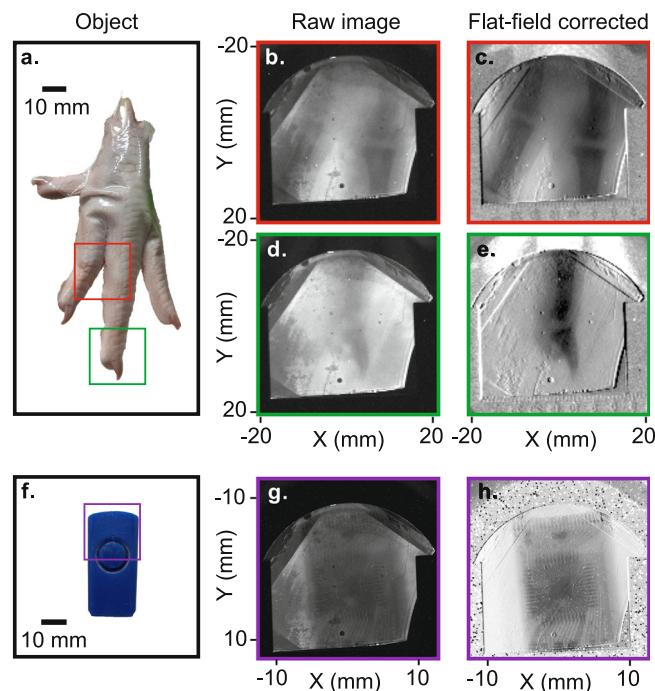


**Fig. 3 | X-ray imaging with large-area nanophotonic scintillators.**

**a, f** Photograph of different objects imaged through our customized imaging setup. The colored square denotes estimated field of views. **b, d, g** Corresponding raw X-ray images. **c, e, h** Corresponding flat-field corrected and contrast-adjusted X-ray images.

Fig. S2)<sup>28,29</sup>. Further discussion of the enhancement mechanism and angular dependence is provided in the SI, Section SI.

We attribute the difference in nanophotonic scintillation enhancement between the two samples to several factors. First, we find in our simulations that thicker scintillators generally exhibit less nanophotonic enhancement, which is consistent with an analysis based on density of states<sup>27,30</sup> (the samples' thickness are  $t_1 = 1$  mm and  $t_2 = 0.5$  mm). Second, we also observe experimentally the influence of different dewetting schemes and mold quality (Compared to the bare scintillator, the coating on the EL sample (respectively, IL sample) slightly reduces (respectively increases) the light out-coupling efficiency. This can be attributed to random pattern formation that occurs when dewetting flat surfaces<sup>31</sup>).

Compared to previous works that aimed at realizing large-area micro or nanostructures on scintillators, our work realizes a six-fold nanophotonic enhancement over a patterned area of  $>1600$  mm<sup>2</sup> (which is only limited by the size of the available scintillator substrates). An overview of the state of the art is shown in Fig. 2e. Previous work with comparably large patterned areas realized enhancements  $\sim 1.3$ . We mainly attribute this five-fold improvement over the state of the art by the use of subwavelength nanophotonic structures. Periodic nanophotonic structures of period  $P$  such that  $\lambda/P \geq 1$  are known to be optimal in terms of density of states enhancement<sup>8,27</sup>. The fact that our method is compatible with patterning of high index, subwavelength structures is therefore key in scaling up nanophotonic scintillator technology to areas required for X-ray imaging applications. While we focus our comparison on the patterned areas, the demonstrated scintillators also improve upon previous nanophotonic scintillators<sup>8,32</sup> by preserving comparable light yield enhancements while increasing thickness by almost an order of magnitude.

### Large-area X-ray imaging

Using the larger area IL sample (4 cm  $\times$  4 cm), we realized X-ray scans of inorganic and organic specimens. The X-ray imaging parameters

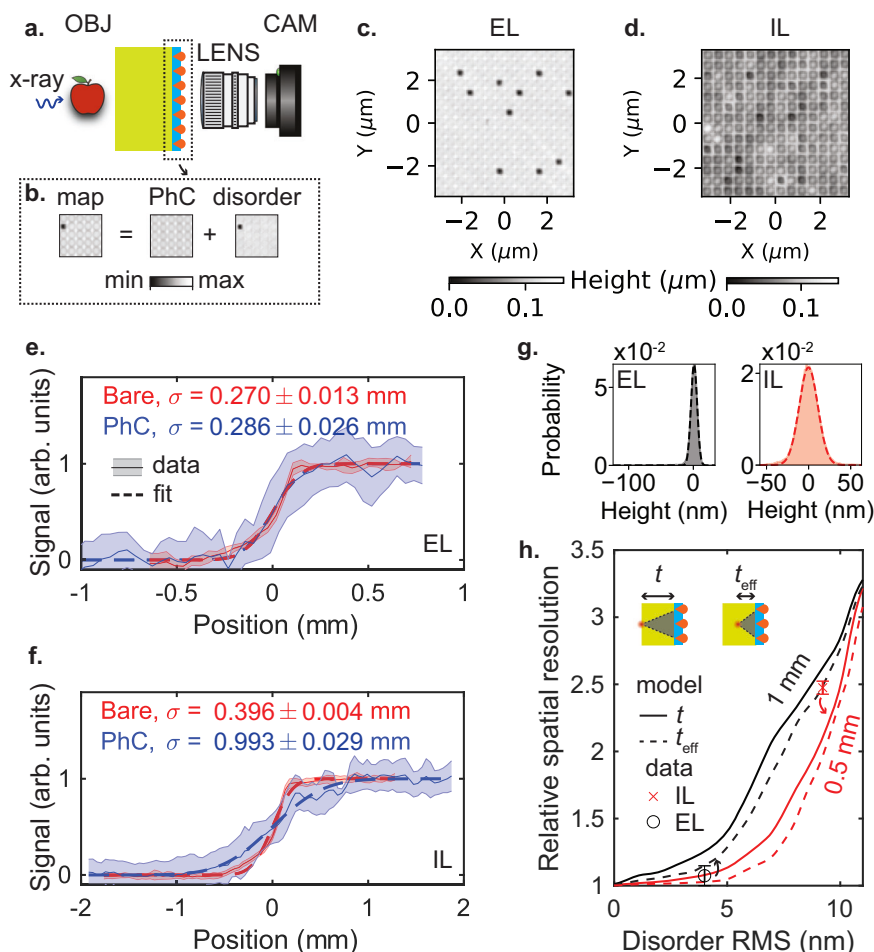


**Fig. 4 | Controlling spatial resolution with disorder in photonic crystal scintillators.** **a** Experimental setup for X-ray imaging with large-area nanophotonic scintillators. OBJ = object; LENS = microscope objective; CAM = CMOS camera. **b** The transfer function of the disordered photonic crystal is modeled as a convolution between that of an ordered photonic crystal and that of a disordered height map. **c, d** Atomic force micrographs (AFM) for EL (**c**) and IL samples (**d**). **e, f** Corresponding spatial resolution measurements in the presence of a razor blade to block part of the incoming X-rays. We note that our imaging system was focused by hand without tracking the position of the focal plane. Therefore, the

focal plane when imaging the EL sample may have been closer to the front (patterned) face of the sample than in the case of the IL sample, resulting in, effectively, lower blur and higher measured spatial resolution. **g** Disorder distribution of the two samples. **h** Relative decrease in spatial resolution (increase in blur) as a function of the disorder root mean square (RMS). Full lines are calculated for fields propagating through the whole scintillator (thickness  $t$ ), dashed lines for its effective thickness  $t_{\text{eff}}$  taking into account X-ray absorption. The dots represent measurements for the two samples (EL and IL) in this paper.

(source voltage and power, as well as geometric and objective magnifications) can be found in the Methods and in the Supplementary Information (SI), Section S4. Each X-ray scan is taken in conjunction with an X-ray flat field image used for post processing, and the final brightness and contrast are digitally adjusted (as would be done in a commercial X-ray scanner for industrial or medical applications).

We first image parts of a chicken foot (tarsometatarsus and digits, shown in Fig. 3a–e). We clearly see several phalanges separated by interphalangeal joints: two proximal and middle phalanges in Fig. 3b, c, and two intermediate and distal phalanges in Fig. 3d, e. We then image a USB stick in Fig. 3f–h and can distinguish multiple levels of printed circuits overlaid on top of each other. These images demonstrate the potential of our scintillators to realize X-ray scans of centimeter-large objects with nanophotonic enhancement.

### Controlling spatial resolution with disorder in photonic crystal scintillators

Next, we elucidate the influence of fabrication disorder on the spatial resolution of nanophotonic scintillators.

When comparing atomic force microscopy (AFM, shown in Fig. 4c, d) images of the two samples, we observe various levels of

disorder which we attribute to different lithography methods used to realize the nanoimprinting mold. A disorder distribution is extracted for both samples using Fourier analysis (see SI, Section S3 and Fig. 4b). We also experimentally characterized each sample's spatial resolution by X-ray imaging the sharp edge of a razor blade, with a setup shown in Fig. 4a. In particular, we fitted an error function to the image of the razor blade and extracted its full width at half maximum (FWHM)  $\sigma$  as a metric of the spatial resolution, although due to the shape of the razor blade's edge, it should not be interpreted as the "true" spatial resolution of the imaging system (further discussion can be found in the SI, Section S4D).

Generally, we observe a correlation between greater amounts of nanofabrication disorder and a decrease in the scintillator's spatial resolution (blur increase). Specifically, the nanofabricated pattern on the EL sample (Fig. 4e) has a spatial resolution of  $\sigma = 0.286 \pm 0.026$  mm, compared to that of a bare, exposed surface on the same sample of  $\sigma = 0.270 \pm 0.013$  mm. This indicates no significant influence on the spatial resolution of the scintillator (with a slight relative decrease within experimental uncertainty). However, the IL sample (Fig. 4f) exhibits a decrease in relative spatial resolution by a factor of  $2.508 \pm 0.099$  (from  $\sigma = 0.993 \pm 0.029$  mm for the patterned

surface to  $\sigma = 0.396 \pm 0.004$  mm for the bare surface). Dependence on the X-ray energy of the spatial resolution is analyzed in the SI, Section S5. A limitation of our measurement of spatial resolution is that our imaging system was focused by hand to achieve the sharpest possible image, without precisely tracking the position of the focal plane. Therefore, it is possible that the focal plane when imaging the EL sample was closer to the front (patterned) facet than the case of the IL sample, resulting in, effectively, lower blur. In the future, this can be mitigated by either tracking the focal plane or keeping it constant between measurements.

To account for the influence of disorder on spatial resolution, we adapted the framework of stochastic surface transfer functions<sup>33</sup> to X-ray scintillation imaging. The disorder distribution from AFM measurements is modeled as a Gaussian-distributed surface transfer function that blurs optical waves incident from within the scintillator. We calculated the relative decrease in spatial resolution for both samples (corresponding to an increase in optical blur, shown in Fig. 4g), with scintillation emission happening on the front facet of the scintillator (propagation through thickness  $t$ ) and at the mean X-ray absorption position (propagation through thickness  $t_{\text{eff}}$ ). The relative decrease in resolution is defined as the ratio of full widths at half maxima of the line spread functions (for a disordered photonic crystal vs. a flat scintillator surface) – a value  $> 1$  corresponding to a decrease in resolution, greater blur, and coarser features of the X-ray scan. These ab initio disorder simulations agree within 7% (comparing data from the EL sample and simulations for  $t_{1,\text{eff}}$ ) and 15% (comparing data from the IL sample and simulations for  $t_{2,\text{eff}}$ ). The remaining discrepancy originates from the uncertainty in the depth at which the imaging objective is focused. More details on the spatial resolution measurement method, disorder modeling, AFM analysis, and calculation of the effective thickness, can be found in the SI, Section S2-3.

Overall, the 0.5-mm patterned scintillator matches the photon yield of a 3-mm unpatterned scintillator ( $\sigma = 2.78$  mm) yet achieves far better resolution ( $\sigma = 0.993 \pm 0.029$  mm). Even with disorder-induced degradation, the resolution still exceeds (about 3-fold) that of a 3-mm unpatterned scintillator (see Fig. S5), overcoming the intrinsic trade-off between light yield and resolution<sup>11,16</sup>.

## Discussion

We have presented a platform for nanophotonic scintillation that combines the following key features: (1) compatibility with greater than centimeter-scale fabrication methods, to enable large-area X-ray imaging; (2) subwavelength feature sizes, to maximize nanophotonic outcoupling<sup>8,27</sup>; (3) absence of residual layer, which may reduce nanophotonic enhancement due to impedance mismatch<sup>34</sup>; (4) ability to realize low-loss high-index ( $n > 2$ ) nanostructures, for greater nanophotonic control<sup>25,35</sup>; (5) high repeatability since a master mold can be used to generate thousands or tens of thousands of large-area nanophotonic scintillators<sup>36,37</sup>. The combination of these factors allowed us to demonstrate scintillation enhancement over scales commensurate with that of commercial X-ray flat panel detectors and provides a path towards their mass production. Unlike bulk nanomaterial-based scintillators, where self-absorption may limit light collection, our approach minimizes this effect by restricting patterning to a very shallow surface layer while preserving bulk scintillator absorption efficiency.

We have also established a clear correlation between nanofabrication disorder and spatial resolution decrease. Improvements in mold quality realized with interference lithography will lead to lower amounts of nanofabrication disorder and little to no decrease in the scintillator's spatial resolution, while improving scintillation light yield six-fold.

Our work is also a first step towards the realization of large-scale metaoptics on scintillators, since the realized method is amenable to local control of the spheroid's shape and induced phase shift<sup>25</sup>. Proper

design and optimization of metasurface masks could lead to coincident enhancements in spatial resolution and light yield<sup>11</sup>, as well as local control of the surface's transfer function<sup>35,38–40</sup>.

Furthermore, the inherent scalability of our fabrication technique opens the door to patterning entire rolls of scintillator materials, paving the way for rapid and affordable mass manufacturing of nanophotonic scintillators. Our method is in principle substrate agnostic, as long as patterns with subwavelength periodicity<sup>27</sup> (compared to the scintillator emission wavelength) can be realized with the master mold. By enabling nanoscale control over electromagnetic properties with controllable disorder, our method ensures both high performance and robustness in practical applications. These developments hold the potential to advance X-ray imaging, as they allow for the integration of complex nanophotonic structures over large areas without compromising quality or significantly increasing costs. These improvements may facilitate the wider adoption of nanophotonic scintillators in various fields requiring high-resolution, high-sensitivity detection of X-rays and other high-energy particles.

## Methods

### Templated dewetting of chalcogenide on scintillator materials

**Mold Fabrication.** Two separate molds are prepared for nanoimprinting. A first mold (Mold 1) is prepared by electron beam lithography over an area of 4 mm × 4 mm. Following oxygen plasma cleaning and HMDS monolayer deposition, a negative electron beam resist (maN 2403, MicroResist Technology GmbH, Germany) is spun at 3000 rpm on a silicon wafer covered with a 30 nm native oxide. The resist is soft baked at 90 °C for 2 min. An inverted grid pattern is written using a 50 keV electron beam and 10 nA current. The resist is developed using a TMAH-based developer (AZ-726, MicroChemicals GmbH, Germany) for 2 min. The native oxide is selectively etched using ICP reactive ion etching (RIE 230iP, Samco, Japan) with fluorine chemistry. A second mold (Mold 2) is prepared by interference lithography over an area of 40 mm × 40 mm. A HeCd laser source ( $\lambda = 325$  nm) is directed at a pinhole placed approximately 60 cm away from a Lloyd's mirror setup. An antireflective coating layer is spun at 3500 rpm onto a silicon wafer with a 30 nm native oxide (AZ Barli II 90, iMicroMaterials, Germany), and baked at 180 °C for 1 min. A layer of positive photoresist (AZ 3312, iMicroMaterials, Germany) is spun at 5000 rpm over the antireflective coating, followed by a soft bake at 110 °C for 1 min. The second mold is exposed with an MLA 150 Advanced Maskless Aligner (Heidelberg Instruments, Germany) at 135  $\mu\text{C}/\text{cm}^2$ , followed by a post-exposure bake at 110 °C for 2 min. The photoresist is developed in AZ 726 for 2 min. The native oxide and antireflective coating are etched using ICP reactive ion etching (RIE 230iP, Samco, Japan) with fluorine chemistry. Both resulting molds are then stripped with an oxygen plasma cleaning step (e3511 Plasma Asher, ESI, USA). The resulting silicon wafer is placed in a 25% KOH solution at 60 °C for anisotropic silicon etching for 2 min. The native oxide hard mask is stripped with a 1 min dip in diluted HF 10: 1.

**Nanoimprint Lithography.** The resulting silicon mold is treated with an anti-sticking layer (Trichloro(1H,1H,2H,2H-perfluorooctyl)silane, Millipore Sigma, USA) in a vacuum desiccator following a short oxygen plasma surface activation. A (poly)dimethylsiloxane layer (PDMS Sylgard 184, Corning, USA) is drop-casted on the silanized mold and cured at 80 °C for 2 h. Upon curing, the PDMS layer is peeled off from the mold.

**Scintillator Patterning.** A thin layer of diluted UV-Curable polymer (Ormocer, MicroResist Technology, Germany) is spun onto the YAG:Ce bulk scintillator. The PDMS nanoimprint mold is pressed directly onto the thin polymer layer. A UV light source ( $\lambda = 375$  nm) is shone through the PDMS to cure the polymer film, with a dose  $>1500$   $\text{mJ}/\text{cm}^2$ . A sub-100 nm thin chalcogenide layer is deposited by thermal evaporation

(PVD Products, USA) directly onto the patterned polymer film. The chalcogenide is annealed above its glass transition temperature to dewet according to the underlying texture. A 15 nm SiO<sub>2</sub> layer is sputtered over the resulting chalcogenide nanoparticle array to protect it from the surrounding oxidative environment (ATC Sputtering System, AJA International, USA).

### X-ray imaging experiments

All experiments, including imaging and measurements of scintillation enhancement and spatial resolution, were done using a custom-built experimental setup inside of a ZEISS Xradia Versa 620 micro-CT. Images were captured using a Hamamatsu ORCA-Fusion C14440-20UP CMOS camera along with a wide-field-of-view camera lens (Edmund Optics 33-304). A narrow bandpass filter centered at 550 nm (AVR Optics FF01-560/14-25, 14 nm bandwidth) was placed in front of the camera lens to minimize unwanted background from other wavelengths. In all experiments, the source was  $d_s = 150$  mm away from the scintillator, while the object distance  $d_o$  depended on the desired geometric magnification of each image, defined as  $M_g = d_s/d_o$ . Here, we summarize the most important details of each experiment; further details of the experimental setup, methods, underlying theory, and data processing can be found in the SI.

**Scintillation enhancement.** Scintillation enhancement was measured by directly imaging the scintillator under excitation from X-rays, comparing patterned and unpatterned areas of the same sample. The line profiles shown in Fig. 2 were extracted from these images. The EL sample was excited by X-rays at 60 kVp and 6.5 W, while the IL sample was excited by X-rays at 150 kVp and 23 W. The scintillation enhancement is calculated using the formula  $(I_p - I_B)/(I_U - I_B)$ , where  $I_p$ ,  $I_U$ ,  $I_B$  are the average patterned, unpatterned, and background intensities from the line profile.

**Imaging.** To capture an image, an object was placed between the source and the scintillator. For each object, the focal plane—usually somewhere inside the scintillator rather than coplanar with the patterned surface—was adjusted by slightly moving the camera lens back and forth to capture the sharpest image. Brightness and contrast were adjusted by carefully tuning the X-ray energy (i.e., kVp), exposure time, and pixel binning and subarray. Figure 3b, d were captured under the following conditions: X-ray energy and power of 30 kVp and 2 W, exposure time of 10 s, binning of 4, and subarray of  $144 \times 144$ , and geometric magnification of 1.2. Finally, Fig. 3g was captured under the following conditions: X-ray energy and power of 60 kVp and 6.5 W, exposure time of 7 s, binning of 1, subarray of  $576 \times 576$ , and geometric magnification of 2. Post-processing included flat-field correction and digitally adjusting brightness and contrast (Fig. 3c, e, and h). The flat-fields were captured by simply removing the objects without changing any of the aforementioned parameters. The chicken foot used in this study was obtained from a local grocery store and prepared for X-ray imaging following standard procedures, including vacuum sealing in a plastic bag to prevent contamination. The USB stick was a 3.0 USB Flash Drive Pen from OneSquareCore.

**Spatial resolution.** The spatial resolutions of the nanophotonic scintillators were estimated by imaging a carbon steel razor blade. Ideally, a region of interest drawn across the edge of the razor blade looks like a blurred, two-dimensional step function that can be reasonably approximated by an edge spread function (ESF) of the form  $ESF(x, y) = (A/2)\text{erf}[(x - \mu)/\sqrt{2}\sigma]$ , where the spatial resolution is  $2\sqrt{2}\ln 2\sigma \approx 2.3548\sigma$ . By fitting the raw data (not the flat-field corrected data, which may remove the effects of blurring due to thickness),  $\sigma$  can be estimated. In Fig. 4e–f, the measured ESFs were captured under the following conditions: X-ray energy and power of 90 kVp and 12 W, exposure time of 3 s, binning of 1, and geometric

magnification of 2. The EL sample (Fig. 4e) used a subarray of  $144 \times 144$ , while the IL sample (Fig. 4f) used a subarray of  $576 \times 576$ .

### Modeling nanophotonic enhancement

**Finite element + rigorous coupled wave analysis modeling.** The nanophotonic scintillation enhancement is modeled using a three-step approach. The large thickness (~mm) of the scintillator and the complex geometry of the nanophotonic structure make it challenging to use a single computational tool with high efficiency and low computational cost. Therefore, a combination of finite element (FE) and rigorous coupled wave analysis (RCWA) methods is employed. The nanophotonic scintillator consists of a chalcogenide spheroid with a diameter of about 395 nm, a subwavelength period of 450 nm, a polymer coating of 450 nm thickness, and scintillator substrate. The refractive index of SiO<sub>2</sub> is obtained from literature<sup>41</sup>, while that of the Ormocer polymer (L5) and YAG:Ce are given by the suppliers. The refractive index of chalcogenide is obtained from in-house ellipsometry measurements (see SI, Fig. S2). All calculations were carried out in the wavelength range of 540 to 560 nm, with the YAG:Ce emission peak centered at 550 nm.

We utilize a commercially available FE solver, COMSOL Multiphysics®, to model the electromagnetic response of the spheroid nanophotonic structure. Initially, we simulate the superstrate without YAG:Ce (polymer coating and chalcogenide spheroid), then combine it with a thinner (1 μm) YAG:Ce scintillator to optimize the geometry. Next, we replace the spheroids with multiple stacked cylinders that approximate the electromagnetic response (transmission and reflection) of the full spheroid structure calculated in the first step (still with an FE solver). This is so that we can shift from FE simulations—where simulating a thick substrate would be difficult to model—to RCWA simulations, where we can use our approximated structure and a thick substrate since it is a semianalytical method. In the third step, we use an automatically differentiable RCWA solver<sup>26</sup>, to simulate the approximate geometry with the thick substrate. The absorption/emission (via reciprocity) within/from the volume of the scintillator is calculated for both polarizations (transverse electric (TE) and transverse magnetic (TM)) and averaged to mimic unpolarized light. Finally, we calculate the enhancement factor as the ratio of the spectrally integrated emission of the patterned scintillator to the unpatterned scintillator.

**Influence of disorder on spatial resolution.** The image degradation due to disorder within the nanophotonic structure is analyzed using surface scatter theory based on the linear shift-invariant system formulation<sup>42</sup>. This is executed in several steps, following traditional image formation theory. First, the modulation transfer function (MTF) of the nanophotonic spheroids is calculated using the transfer function retrieved directly from the transmission as a function of angle (using RCWA). Consequently, the disorder is modeled using the surface scatter theory to calculate the surface transfer function (STF). The scattering property by the disorder (defects) is considered in transmission mode to formulate the STF (see SI, Section S2). Here, we utilize a Gaussian autocovariance function with surface roughness root mean square (RMS) retrieved from AFM images using Fourier analysis (see SI, Section S3).

Further, we define the system modulation transfer function (MTFsys), which incorporates the influence of nanophotonic spheroids and disorder, via the two transfer functions: MTF and STF (multiplication in the Fourier space). MTFsys provides a complete linear system formulation of image quality as degraded by surface scatter effects due to disorder from residual optical fabrication errors. Once the MTFsys is derived, we proceed to obtain the line spread function (LSF) through an inverse Fourier transform to real space. This is followed by propagation through the optical imaging setup, encompassing free space and optical components. The full width at half

maximum (FWHM) of the LSF serves as the defining measure of the system's resolution. These procedures are consistently applied to both EL and IL samples in both effective (0.76, 0.36 mm) and real (1, 0.5 mm) thicknesses (see definition of the effective thickness in SI, Section S2). Subsequently, the FWHM of the nanophotonic structure is compared with that of a smooth unpatterned scintillator to calculate the relative spatial resolution as a function of RMS (1–11 nm). The calculations above are performed by considering the peak emission wavelength (550 nm) of the scintillator.

### Data availability

The experimental and simulation data generated in this study have been deposited on a repository accessible on Zenodo<sup>43</sup> (<https://doi.org/10.5281/zenodo.15302479>). This repository contains the data used to generate the plots in Fig. 2–4. Correspondence and requests for materials should be addressed to L.M.M. (lmmartin@mit.edu), S.P. (pajovics@mit.edu), M.G.A. (MulunehGeremew.ABEBE@umons.ac.be), and C.R.-C. (chrc@stanford.edu).

### Code availability

The scripts used to implement the model used in this study are available from the corresponding authors upon request.

### References

- Gektin, A. & Korzhik, M. Inorganic scintillators for detector systems. *Berlin: Springer* 20–77 (2017).
- Nagarkar, V. et al. A new large area scintillator screen for X-ray imaging. *Nucl. Instrum. Methods Phys. Res. Sect. B: Beam Interact. Mater. At.* **213**, 250–254 (2004).
- Yoshikawa, A., Chani, V. & Nikl, M. Czochralski growth and properties of scintillating crystals. *Acta Phys. polonica A* **124**, 250–264 (2013).
- Boatner, L. A. et al. Advances in the growth of alkaline-earth halide single crystals for scintillator detectors. In *Hard X-Ray, Gamma-Ray, and Neutron Detector Physics XVI*, vol. 9213, 88–98 (SPIE, 2014).
- Cha, B. K., Kim, J. Y., Kim, T. J., Sim, C. & Cho, G. Fabrication and imaging characterization of high sensitive CsI (Tl) and Gd<sub>2</sub>O<sub>2</sub>S (Tb) scintillator screens for X-ray imaging detectors. *Radiat. Meas.* **45**, 742–745 (2010).
- Bhandari, H. B. et al. Hot wall evaporation of high-sensitivity, high-resolution CeBr<sub>3</sub> scintillator. *IEEE Trans. Nucl. Sci.* **59**, 2196–2200 (2012).
- Nedelec, J.-M. Sol-gel processing of nanostructured inorganic scintillating materials. *J. Nanomaterials* **2007**, 036392 (2007).
- Roques-Carmes, C. et al. A framework for scintillation in nanophotonics. *Science* **375** (2022).
- Kurman, Y., Shultzman, A., Segal, O., Pick, A. & Kaminer, I. Photonic-crystal scintillators: Molding the flow of light to enhance X-ray and  $\gamma$ -ray detection. *Phys. Rev. Lett.* **125**, 040801 (2020).
- Knapitsch, A. & Lecoq, P. Review on photonic crystal coatings for scintillators. *Int. J. Mod. Phys. A* **29**, 639–643 (2014).
- Shultzman, A., Segal, O., Kurman, Y., Roques-Carmes, C. & Kaminer, I. Enhanced imaging using inverse design of nanophotonic scintillators. *Adv. Optical Mater.* **11**, 2202318 (2023).
- Ye, W., Bizarri, G., Birowosuto, M. D. & Wong, L. J. Enhancing large-area scintillator detection with photonic crystal cavities. *ACS Photonics* **9**, 3917–3925 (2022).
- Li, Z. et al. Fabrication of large-area photonic crystal-modified x-ray scintillator imager for optical coding imaging. *Opt. Express* **32**, 8877–8886 (2024).
- Ye, W. et al. The nanoplasmonic purcell effect in ultrafast and high-light-yield perovskite scintillators. *Adv. Mater.* 2309410 (2024).
- Roques-Carmes, C. et al. Free-electron–light interactions in nanophotonics. *Appl. Phys. Rev.* **10** (2023).
- Singh, P., Dosovitskiy, G. & Bekenstein, Y. Bright innovations: Review of next-generation advances in scintillator engineering. *ACS nano* (2024).
- Shultzman, A. et al. Towards a second generation of metascintillators using the purcell effect. *IEEE Transactions on Radiation and Plasma Medical Sciences* 1–1 (2024).
- Tseng, A. A., Chen, K., Chen, C. D. & Ma, K. J. Electron beam lithography in nanoscale fabrication: recent development. *IEEE Trans. Electron. Packaging Manuf.* **26**, 141–149 (2003).
- Zywietz, U., Evlyukhin, A. B., Reinhardt, C. & Chichkov, B. N. Laser printing of silicon nanoparticles with resonant optical electric and magnetic responses. *Nat. Commun.* **5**, 1–7 (2014).
- Urban, A., Lutich, A., Stefani, F. & Feldmann, J. Laser printing single gold nanoparticles. *Nano Lett.* **10**, 4794–4798 (2010).
- Fan, J. A. et al. Self-assembled plasmonic nanoparticle clusters. *Science* **328**, 1135–1138 (2010).
- Vigderman, L., Khanal, B. & Zubarev, E. Functional gold nanorods: synthesis, self-assembly, and sensing applications. *Adv. Mater.* **24**, 4811–4841 (2012).
- Flauraud, V. et al. Nanoscale topographical control of capillary assembly of nanoparticles. *Nat. Nanotechnol.* **12**, 73–80 (2016).
- Zakery, A. & Elliott, S. Optical properties and applications of chalcogenide glasses: a review. *J. Non-Crystalline Solids* **330**, 1–12 (2003).
- Das Gupta, T. et al. Self-assembly of nanostructured glass metasurfaces via templated fluid instabilities. *Nat. Nanotechnol.* **14**, 320–327 (2019).
- Jin, W., Li, W., Orenstein, M. & Fan, S. Inverse design of lightweight broadband reflector for relativistic lightsail propulsion. *ACS Photonics* **7**, 2350–2355 (2020).
- Yu, Z., Raman, A. & Fan, S. Fundamental limit of nanophotonic light trapping in solar cells. *Proc. Natl. Acad. Sci. USA* **107**, 17491–17496 (2010).
- Yu, Z., Raman, A. & Fan, S. Fundamental limit of light trapping in grating structures. *Opt. Express* **18**, A366–A380 (2010).
- Yu, Z. & Fan, S. Angular constraint on light-trapping absorption enhancement in solar cells. *Appl. Phys. Lett.* **98** (2011).
- Benzaouia, M. & Fan, S. Theory for broadband large-area purcell enhancement. *ACS Photonics* **11**, 2667–2672 (2024).
- Xue, L. & Han, Y. Pattern formation by dewetting of polymer thin film. *Prog. Polym. Sci.* **36**, 269–293 (2011).
- Kurman, Y. et al. Purcell-enhanced x-ray scintillation. *Sci. Adv.* **10**, eadq6325 (2024).
- Harvey, J. E. Parametric analysis of the effect of scattered light upon the modulation transfer function. *Optical Eng.* **52**, 073110–073110 (2013).
- Choi, H. et al. Realization of high aspect ratio metalenses by facile nanoimprint lithography using water-soluble stamps. *Photonix* **4**, 18 (2023).
- Khorasaninejad, M. et al. Metalenses at visible wavelengths: diffraction-limited focusing and subwavelength resolution imaging. *Science* **352**, 1190–1194 (2016).
- Guo, L. J. Nanoimprint lithography: methods and material requirements. *Adv. Mater.* **19**, 495–513 (2007).
- Chou, S. Y., Krauss, P. R. & Renstrom, P. J. Nanoimprint lithography. *J. Vac. Sci. Technol. B: Microelectron. Nanometer Struct. Process. Meas. Phenom.* **14**, 4129–4133 (1996).
- Yu, N. et al. Light propagation with phase discontinuities: generalized laws of reflection and refraction. *Science* **334**, 333–337 (2011).
- Yu, N. & Capasso, F. Flat optics with designer metasurfaces. *Nat. Mater.* **13**, 139–150 (2014).
- Overvig, A. C., Mann, S. A. & Alù, A. Thermal metasurfaces: complete emission control by combining local and nonlocal light-matter interactions. *Phys. Rev. X* **11**, 021050 (2021).

41. Rodríguez-de Marcos, L. V., Larruquert, J. I., Méndez, J. A. & Aznárez, J. A. Self-consistent optical constants of SiO<sub>2</sub> and Ta<sub>2</sub>O<sub>5</sub> films. *Optical Mater. Express* **6**, 3622–3637 (2016).
42. Harvey, J. E. Retrospective of Roland Shack's global view of diffraction. *Appl. Opt.* **59**, G185–G203 (2020).
43. Roques-Carmes, C., Martin-Monier, L., Pajovic, S. & Abebe, M. G. Data repository for "Large-scale self-assembled nanophotonic scintillators for X-ray imaging" (2025, Zenodo, <https://doi.org/10.5281/zenodo.15302479>).
44. Salomoni, M. et al. Photonic crystal slabs applied to inorganic scintillators. *IEEE Trans. Nucl. Sci.* **12**, 15 (2017).
45. Salomoni, M., Pots, R., Auffray, E. & Lecoq, P. Enhancing light extraction of inorganic scintillators using photonic crystals. *Crystals* **8** (2018).
46. Zanettini, S. et al. Improved light extraction efficiency on 2 inches LYSO with nanopatterned TiO<sub>2</sub> photonic crystals. In *IEEE Strasbourg* (2016). Available online: <https://www.silsef.com/Documents.htm> (accessed on 29 December 2017).
47. Liu, J. et al. Modified timing characteristic of a scintillation detection system with photonic crystal structures. *Opt. Lett.* **42**, 987–990 (2017).
48. Zhang, J. et al. Enhanced light extraction of LYSO scintillator by photonic crystal structures from a modified porous anodized aluminum oxide layer. *Nucl. Instrum. Methods Phys. Res. Sect. A* **864**, 36–39 (2017).
49. Zhu, Z. et al. Improvement of light extraction of LYSO scintillator by using a combination of self-assembly of nanospheres and atomic layer deposition. *Opt. Soc. Am.* **23**, 7085–7093 (2015).
50. Zhu, Z. et al. Improved light extraction of LYSO scintillator by the photonic structure from a layer of anodized aluminum oxide. *Nucl. Instrum. Methods Phys. Res. Sect. A* **786**, 1–4 (2015).
51. Zhu, Z. et al. Enhanced light extraction of scintillator using large-area photonic crystal structures fabricated by soft-X-ray interference lithography. *Appl. Phys. Lett.* **106** (2015).
52. Chen, X. et al. Enhanced light extraction of plastic scintillator using large-area photonic crystal structures fabricated by hot embossing. *Opt. Express* **26**, 11438–11446 (2018).

## Acknowledgements

We would like to thank Paul Lecoq, Ido Kaminer, Irina Shestakova, Olivier Philip, Bipin Singh, and Vivek Nagarkar for stimulating discussions. We thank Tim Savas for advice on interference lithography and Chris Hogan for experimental assistance. The authors thank Dr. Svetlana V. Boriskina for access to a 3D printer. This work is supported in part by the DARPA Agreement No. HO0011249049, as well as being also supported in part by the U. S. Army Research Office through the Institute for Soldier Nanotechnologies at MIT, under Collaborative Agreement Number W911NF-23-2-0121. L.M.M. was supported by the DARPA ENvision program and a fellowship from the Swiss National Science Foundation (P500PT-203222). S. P. gratefully acknowledges support from the NSF GRFP under Grant No. 2141064. M.G.A. is funded by the Fonds de la Recherche Scientifique - FNRS (Grant No. FC 053809) and Wallonie-Bruxelles International (WBI) fellowship. C.R.-C. is supported by a Stanford Science Fellowship.

## Author contributions

L.M.-M. and C.R.-C. conceived the original idea. L.M.-M. developed the fabrication methods. S.P. built the experimental setup and acquired the data with contributions from J.C., L.M.-M., S.V., S.E.K., and C.R.-C. Experimental data and processing were performed by S.P., M.G.A., and C.R.-C. Sample characterization (scanning electron and atomic force micrographs) were obtained by L.M.-M. and S.E.K. M.G.A. performed the numerical simulations with contributions from L.M.-M., S.P., J.C., S.V., S.M., S.C., and C.R.-C. C.R.-C., M.S., J.H., and B.M. supervised the project. The manuscript was written by L.M.-M., S.P., M.G.A., and C.R.-C. with inputs from all authors.

## Competing interests

S.E.K., M.S., and C.R.-C. are seeking patent protection for ideas in this work (US Patent Application 18/286,808). M.S. and C.R.-C. are seeking patent protection for ideas in this work (provisional patent application no. 63/257,611). L.M.-M., S.P., J.H., M.S., and C.R.-C. are seeking patent protection for ideas in this work (provisional patent applications no. 63/778,698). The remaining authors declare no competing interests.

## Additional information

**Supplementary information** The online version contains supplementary material available at <https://doi.org/10.1038/s41467-025-60953-5>.

**Correspondence** and requests for materials should be addressed to Louis Martin-Monier, Simo Pajovic, Muluneh G. Abebe or Charles Roques-Carmes.

**Peer review information** *Nature Communications* thanks Bo Liu, Huanghao Yang and the other anonymous reviewer(s) for their contribution to the peer review of this work. A peer review file is available.

**Reprints and permissions information** is available at <http://www.nature.com/reprints>

**Publisher's note** Springer Nature remains neutral with regard to jurisdictional claims in published maps and institutional affiliations.

**Open Access** This article is licensed under a Creative Commons Attribution-NonCommercial-NoDerivatives 4.0 International License, which permits any non-commercial use, sharing, distribution and reproduction in any medium or format, as long as you give appropriate credit to the original author(s) and the source, provide a link to the Creative Commons licence, and indicate if you modified the licensed material. You do not have permission under this licence to share adapted material derived from this article or parts of it. The images or other third party material in this article are included in the article's Creative Commons licence, unless indicated otherwise in a credit line to the material. If material is not included in the article's Creative Commons licence and your intended use is not permitted by statutory regulation or exceeds the permitted use, you will need to obtain permission directly from the copyright holder. To view a copy of this licence, visit <http://creativecommons.org/licenses/by-nc-nd/4.0/>.

© The Author(s) 2025